Vanadium Diphosphide as a Negative Electrode Material for Sodium Secondary Batteries

Shubham Kaushik[a], Kazuhiko Matsumoto[a,b,*], Yuki Orikasa[c], Misaki Katayama[c], Yasuhiro Inada[c], Yuta Sato[d], Kazuma Gotoh[b,e], Hideka Ando[e] and Rika Hagiwara[a,b]

[a]Graduate School of Energy Science, Kyoto University, Sakyo-ku, Kyoto 606-8501, Japan

[b]Unit of Elements Strategy Initiative for Catalysts & Batteries (ESICB), Kyoto University, Katsura, Kyoto 615-8510, Japan

[c]Department of Applied Chemistry, Ritsumeikan University, 1-1-1 Noji-higashi, Kusatsu Shiga 525-8577, Japan

[d]Nanomaterials Research Institute Institution, National Institute of Advanced Industrial Science and Technology (AIST), Central 5, 1-1-1 Higashi, Tsukuba, Ibaraki 305-8565, Japan

[e]Graduate School of Natural Science & Technology, Okayama University, 3-1-1 Tsushima-naka, Okayama 700-8530, Japan

*Corresponding Author E-mail Address: k-matsumoto@energy.kyoto-u.ac.jp

Abstract

The abundance of sodium resources has sparked interest in the development of sodium-ion batteries for large-scale energy storage systems, amplifying the need for high-performance negative electrodes. Although transition metal phosphide electrodes have shown remarkable performance and great versatility for both lithium and sodium batteries, their electrochemical mechanisms in sodium batteries, particularly vanadium phosphides, remain largely elusive. Herein, we delineate the performance of VP_2 as a negative electrode alongside ionic liquids in sodium-ion batteries. The polycrystalline VP_2 is synthesized via one-step high energy ball-milling and characterized using X-ray diffraction, X-ray photoelectron spectroscopy, and transmission electron microscopy. Electrochemical tests ascertained improved performance at intermediate temperatures, where the initial cycle was conducted at 100 mA g^{-1} yielded a significantly higher discharge capacity of 243 mAh g^{-1} at 90 °C compared to the limited capacity of 49 mAh g^{-1} at 25 °C. Enhanced rate and cycle performance are also achieved at 90 °C. Electrochemical impedance spectroscopy and scanning electron microscopy further reveal a reduced charge transfer resistance at 90 °C and the formation of a uniform and stable solid electrolyte interface (SEI) layer after cycling. X-ray diffraction and nuclear magnetic resonance spectroscopy are used to confirm the conversion-based mechanism forming Na_3P after charging.

Introduction

Giant leaps in the augmentation of renewable energy sources, in particular, solar and wind, have brought to light the pivotal role of energy storage systems in addressing the intermittency of these alternative energy sources [1, 2]. As a result, lithium-ion batteries (LIBs) have gained immense popularity owing to their exceptional energy and power densities, long lifespan and versatility in both large-scale and consumer applications [3-5]. However, scarcity of natural reserves and restrictive costs of LIB components [6] such as lithium, cobalt, and nickel have aroused skepticism in their sustainability, compelling researchers to explore alternative battery chemistries such as sodium-based technologies [7-10]. It is this context, that interest in sodium-ion batteries (NIBs) has rekindled over the last decade [10-14], propelled by the great abundance of sodium reserves on terrestrial surfaces and in seawater [15-19]. Moreover, the low redox potential of Na^+/Na (–2.71 V vs. standard hydrogen electrode) points towards the prospects of developing competitive NIBs with high energy densities [20, 21].

Despite the propitious electrochemistry of NIBs, their advancement is greatly inhibited by incompatibility with conventional negative electrodes such as graphite due to their limited capabilities to facilitate sodium intercalation during battery operations. Even though recent studies have shown reversible Na^+ ion intercalation into graphite induced by co-intercalation of solvent forming complex ($Na^+[(diglyme)_2C_{20}]^-$) [22] that result in larger interlayer distances [23], the limited capacities achieved are inadequate for high energy density NIBs. As an alternative, hard carbons with randomly oriented turbostratic graphene domains, have shown considerable improvement, exhibiting higher reversible capacities and lower operating voltages than graphite [24-26]. A first cycle charge capacity of 430.5 mAh g^{-1} at a rate of 30 mAh g^{-1} was obtained from a biomass-derived hard carbon (HC) prepared by single-step pyrolysis of shaddock peel on account

of their large interlayer distances and honeycomb morphology [27]. However, the safety concerns with hard carbons related to the possible sodium metal deposition due to the sodiation potential close to 0 V vs Na/Na^+, have motivated researchers to explore other materials for negative electrodes for NIBs. Sodium titanates ($Na_2Ti_3O_7$, $Na_2Ti_6O_{13}$) are another prospective class of material providing low voltage for realizing high energy densities for NIBs [28-30].

The binary M_yX_z compounds consisting of the 3d transition metals (M) and main group element (X) have emerged as versatile negative electrode materials, showing different charge-discharge mechanisms in both LIBs and NIBs, depending on their combinations [31]. For instance, an early 3d transition metal oxide, TiO_2, operates as a topotactic insertion-type electrode in LIBs [32] but can facilitate conversion-type mechanism in NIBs [33]. On the other hand, the later 3d transition metal oxide CuO, has been found to shows conversion mechanisms in both LIBs and NIBs [34].

Within this class of materials, metal phosphides have emerged as a promising electrode material candidates, showing high theoretical capacities in both weight and volume [35-37]. A tin phosphide electrode (Sn_4P_3) prepared by ball-milling showed a high capacity of 718 mAh g^{-1} at 100 mA g^{-1} with negligible capacity fading over 100 cycles of NIB operations. The remarkable performance was largely attributed to the confinement of Sn nanocrystallites in the amorphous phosphorus matrix [38]. Similarly, a copper phosphide carbon composite (CuP_2/C) also prepared through high energy ball-milling, achieved a reversible capacity of 450 mAh g^{-1} with a high capacity retention of 95% after 100 cycles of NIB operations [39]. Ex-situ XRD analyses revealed the formation of Na_3P and reversible formation of CuP_2 after sodiation and desodaition, respectively. Due to their superior performance, numerous reports that comprehensively detail the electrochemical performance of phosphorus and phosphide in NIBs have been availed [40, 41].

Vanadium phosphides (V_xP_y) are known to their diverse electrochemistry in secondary batteries [42-44]. For instance, V_4P_7 prepared by high-energy ball-milling (HEBM) shows topotactic insertion of both Na^+ and Li^+ insertion for NIBs [45] and LIBs [46], respectively. Likewise, the performance of a vanadium diphosphide (VP_2) electrode prepared by HEBM and solid-state annealing was investigated for LIBs, yielding superior and showed high discharge capacities of 890 and 640 mAh g^{-1}, respectively [44]. According to X-ray diffraction (XRD) analysis, an amorphous product was observed after lithiation of VP_2 and the redox center at the anion site was proposed because of no change in V *K*-edge spectra in XAFS. Other V_xP_y species such as VP_4, have been found to facilitate both conversion and intercalation reactions during LIB operation. The electrochemical mechanism was determined to entail an initial reaction which resulted in the formation of Li_3P and VP, thereby allowing the subsequent insertion of Li into VP at low voltages [43]. As a result, a significantly higher discharge capacity of 1290 mAh g^{-1} was attained. It can be deduced from the aforementioned studies that increasing phosphorus content in V_xP_y induces conversion-based mechanism. However, in the reported case of VP_4, huge volume fluctuations occurring during the conversion reaction led to capacity fading. Thus, intermediate phosphorus amounts in V_xP_y could be envisaged to exhibit stable cyclability. Although intensive studies and reports on this family of metal phosphides exist, information regarding the charge-discharge mechanism of V_xP_y is not yet well understood.

The choice of electrolyte is deemed a crucial factor dictating not only the electrochemical performance but also the safety of the battery [47]. Among the commonly used electrolytes, organic electrolytes have turned out to be highly flammable and volatile, causing hazardous fires in some batteries [9, 48]. As such, ionic liquid electrolytes (ILs), have emerged as safe electrolyte alternatives for both LIBs and NIBs owing to their high thermal stability, low flammability and

negligible volatility [49-54]. Furthermore, their wide electrochemical windows make them compatible with a variety of negative and positive electrodes in a wide temperature range [55, 56], displaying high performances that in some cases even surpass organic electrolytes [57-62]. Besides, the adoption of IL in NIBs can facilitate stable operations at intermediate temperatures which activate the electrochemical capabilities of certain inactive materials, enabling them to yield unprecedentedly high rate capability [63-66]. The prospect of intermediate-temperature operations also unlock opportunities to take advantage of waste heat from automobiles and large-scale applications.

The ability of IL to induce the formation of uniform and stable solid electrolyte interface (SEI) layer in certain negative electrodes has been known to prompt huge improvements in cyclability and rate capability among NIBs [67-69]. For example, a $FeTiO_3$-C composite negative electrode used alongside Na[FSA]–[C_3C_1pyrr][FSA] (20 : 80 in mol) (FSA^- = bis(fluorosulfonyl)amide and $C_3C_1pyrr^+$ = *N*-methyl-*N*-propylpyrrolidinium) IL, showed excellent cyclability marked by a capacity retention of 113% after 2000 cycles at 90 °C [70]. In a comparative study between IL and organic electrolyte, red phosphorus-acetylene black (AB) composite prepared by ball-milling exhibited better cyclability during IL operations [71]. This was ascribed to the differences in the SEI components formed by the two electrolytes, with IL producing a more robust SEI as was revealed by hard X-ray photoelectron spectroscopy and time-of-flight secondary ion mass spectroscopy. Similarly, the SEI layer on HC using 1 M Na[FSA]–[C_3C_1pyrr][FSA] IL and 1 M Na[ClO_4]–EC: DEC (1:1 v/v) (EC = ethylene carbonate and DEC = diethyl carbonate) was systematically investigated at 25 °C using electrochemical impedance spectroscopy (EIS) and X-ray photoelectron spectroscopy (XPS) [72]. The HC/HC symmetric cell showed significantly lower charge transfer resistance in the case of IL compared to organic

electrolyte owing to a thinner SEI layer in IL electrolyte. In another case, during an investigation of vanadium phosphide-phosphorus composite (V_4P_7-5P) negative electrode utilizing 1 M Na[FSA]–[C_3C_1pyrr][FSA] IL at 25 and 90 °C, a stable cyclability was observed in the course of 100 cycles [73]. However, severe capacity degradation occurred when the electrode was operated in 1 M Na[PF_6]–EC:DEC (1:1 v/v) organic electrolyte, as was reflected by increasing impedance as cycling progressed.

In this study, the electrochemical performance of VP_2 is investigated using 1 M Na[FSA]–[C_3C_1pyrr][FSA] IL for NIBs at 25 and 90 °C. The electrode material was prepared by a one-step HEBM at 850 rpm for 20 h and further characterized by XRD, XPS and transmission electron microscopy (TEM). The performance was thereafter validated using EIS and scanning electron microscopy (SEM) upon cycling. The charge-discharge mechanism is ascertained using ex-situ XRD, XPS, and X-ray absorption fine structure (XAFS) and magic angle spinning nuclear magnetic resonance (MAS NMR) spectroscopic analysis.

Experimental

All the air-sensitive materials were handled in an Ar-filled glove box (H_2O < 1 ppm, O_2 < 1 ppm). Vanadium (Kojundo Chemical Lab, purity 99.9%) and phosphorus (Wako Pure Chemical Industries, purity 98%) powders were ball-milled using a planetary ball mill (Pulverisette 7 Fritsch) for 20 h at 850 rpm under Ar atmosphere in a 1:2 molar ratio to obtain VP_2 powder. A 20 cm^{-3} grinding bowl with zirconia balls (with diameters of 3 mm) was used. The ball-milling parameters were optimized by changing the operation time and speed to obtain polycrystalline products.

The negative composite electrode was prepared by mixing the active material (VP_2), AB as

conductive additive, and a polyamide-imide (PAI) binder in a 75:15:10 weight ratio in *N*-methyl-2-pyrrolidone (Wako Pure Chemical Industries, purity 99%) solvent. Another composite electrode adopting a ratio of VP_2:AB:PAI as 90:5:5 in weight was used for a control experiment to elucidate the effects of carbon content on the electrochemical behavior. The resulting slurries were cast on Al foils, dried under vacuum at 90 ˚C for 10 h in an oven and subsequently placed in an airtight cell connected to a vacuum line at 110 °C overnight. The mass loading of the active material in the electrode was ~1.5 mg cm^{-2}. The salts, Na[FSA] (Mitsubishi Materials Electronic Chemicals, purity >99%) and [C_3C_1pyrr][FSA] (Kanto Chemical, purity >99.9%), were dried under vacuum at 80 °C for 24 h, followed by mixing of the dried salts in the 20 : 80 molar ratio to prepare the IL electrolyte. An organic electrolyte comprising 1 M $NaPF_6$ in EC:DEC (1:1 v/v) (Battery grade, Kishida Chemical) was also used as-purchased. Glass fiber separators (Whatman, GF-A, 260 mm in thickness and 16 mm in diameter) were dried at 110 °C under vacuum. The separator was impregnated with the IL at 80 °C under vacuum overnight prior to use. Sodium metal (Aldrich, purity 99.9%) was spread into a disc and used as a counter electrode. Coin cells (2032-type) were assembled in the glove box to evaluate the electrochemical performance.

Electrochemical behavior of the prepared electrodes (charge-discharge, rate capability, and cycleability tests) were measured using an HJ1001SD8 charge−discharge test device (Hokuto Denko). All the capacity and current density are described based on the weight of VP_2. The prepared coin cells were kept at an open circuit voltage for more than 3 h prior to the tests. Electrode behavior was analyzed by EIS using a VSP potentiostat (Bio-Logic) at 25 and 90 °C over a frequency range from 100 kHz to 10 mHz with an amplitude of 20 mV. The cells were cycled at the rate of 100 mA g^{-1} for the first three cycles and 500 mA g^{-1} for the subsequent cycles. The EIS spectra were measured at 0.5 V during the charging step of the *n*th cycle (n = 2, 4, 11, 51,

and 101).

The thermal stability of as-prepared VP_2 was assessed by thermogravimetric (TG) analysis (STA2500 Regulus, NETZSCH) at a scan rate of 5 °C min^{-1} under a dry Ar atmosphere. The XRD patterns of the pristine and charged/discharged samples were recorded with a Rigaku SmartLab diffractometer (Cu Kα (λ = 1.5418 Å), 40 kV−30 mA). The sample for ex-situ XRD after electrochemical tests were prepared by disassembling the cells followed by rinsing with tetrahydrofuran (Wako Pure Chemical Industries, water content ≤ 10 ppm) and vacuum-drying for one day at room temperature. Particle size and morphology were analyzed by SEM (Hitachi SU-8020). The sample for SEM after 500 cycles was prepared by applying the same procedures as *ex situ* XRD. Electrode surface was analyzed by XPS using an X-ray photoelectron spectrometer (JEOL, JPS-9010, Mg Kα, 10 kV−10 mA). For the charged/discharged samples, Ar etching was performed at the ion energy of 600 eV for 30, 60, 90, 120 and 180 s. The TEM samples were prepared in a similar manner to that for *ex-situ* XRD, but the powder was scratched from the Al foil after drying. The resulting sample was observed by (scanning) transmission electron microscopy ((S)TEM, JEOL JEM-2100F) at 60 kV. Energy dispersive X-ray spectroscopy (EDX) combined with STEM was performed using double JEOL Centurio detectors attached to the microscope. For X-ray absorption measurements, the electrodes were charged and discharged to 0.005 and 2.0 V, respectively, and scratched from the current collector. The resulting powder was mixed with boron nitride powder and then made into a pellet (10 mm in diameter) prior to measurements. XAFS data were obtained using the beam line BL-3 at the SRcenter, Ritsumeikan University. The V *K*-edge spectra were measured in the transmission mode. Samples for XAFS measurements were treated without air exposure. Solid state ^{31}P NMR spectra were obtained using an NMR system (11.7 T magnet, DD2; Agilent technology Inc.) at a MAS speed of 10 or 12 kHz.

A single pulse sequence with 2.5 μs pulse was applied. $[NH_4]H_2PO_4$ powder was used as an external standard of the chemical shift (1 ppm). The samples for NMR spectroscopy were prepared by disassembling the coin cell without washing the electrode with a solvent.

Results and discussions

The VP_2 sample was prepared via a one-step high energy ball milling (HEBM) of stoichiometric amounts of vanadium and red phosphorus powder at the milling speed of 850 rpm for 20 h using a 50:1 ball-to-powder weight ratio. To determine the optimal conditions for the synthesis of VP_2, XRD patterns of the compounds formed under varying milling times and speeds at a constant ball-to-powder ratio of 50:1 (w/w) were taken as shown in Fig. S1 and S1b, respectively. The patterns (Fig. S1a) indicate that ball milling at 400 rpm yields $VP_{1.75}$ (V_4P_7) [74] (space group: $P\bar{4}m2$), irrespective of the milling time (40, 60, and 80 h). An increase in milling speeds from 600 to 800 rpm results in the formation of a VP_2 [75] (space group: $C2/m$) compounds containing residual amounts of VP [76]. Nevertheless, pure VP_2 is achieved after milling speeds were increased to 850 (Fig. 1). For more details on the crystallographic structures, and electrochemical performance (in both NIBs and LIBs) of the assorted V_xP_y compounds formed under different HEBM conditions, a summary is provided in Table 1.

For further characterization, SEM, TEM, EDX, and XPS analyses were conducted in the as-prepared VP_2. As can be seen in the SEM images obtained (Fig. S2), the particle sizes of the VP_2 compound were found to range from hundreds of nanometers to a few micrometers. The VP_2 compound was also subjected to (S)TEM analysis to investigate the crystal structure of the material as shown in Fig. 2. The polycrystalline nature of the material is manifested by bright spots appearing in a circular path (Debye-Scherrer rings) as illustrated by the selected area electron

diffraction (SAED) pattern obtained from pristine VP_2 (Fig. 2a). This deduction is further validated by the light and dark contrast in the high-resolution (HR) TEM image (Fig. 2b). Moreover, from the HRTEM image the crystallite size is discerned to fall in the 8 to 20 nm range, in conformity with the estimation derived from the XRD peaks using the Scherrer equation (details furnished in the Supplementary Information). STEM-EDX mapping performed on the material displays a consistent contrast throughout the particle, portraying the homogenous distribution of P and V elements (Fig. 2c). A magnification of the HRTEM image allows a clear visualization of the lattice fringes of VP_2 as seen in Fig. 2d. As is typical, to determine the *d*-spacing from the HRTEM image of VP_2 (Fig. 2d), the fast Fourier transform (FFT) power spectrum was employed [77]. The crystallite *d*-spacings were discerned to be 0.25 and 0.19 nm which correspond to the strongest and second strongest diffraction peaks indexed at 111 and 310, respectively in the XRD pattern of the VP_2 compound. Additionally, XPS spectra of the pristine VP_2 powder were derived as shown in Fig. S3. In the P 2p region, two broad peaks assignable to the V−P bonds in VP_2 [75] and the P−O bonds on the surface of the sample [39], were observed at 128.8 and 133.4 eV, respectively; an indication of phosphorus oxidation during the ball-milling process (Fig. S3a). Similarly, a strong peak assignable to a V−P bond [78] is identified at 512.4 eV alongside weak peaks indexable to VO_x [79, 80] in the V 2p region (Fig. S3b) that corresponds to higher binding energies. Similar peaks are also seen in the V 2p and P 2p XPS spectra of the $VP_{1.75}$ reported earlier [45]. To confirm whether any residual elemental phosphorous was present, the VP_2 powder was placed in an Ar atmosphere and temperature was raised from room temperature to 500 °C at a ramp rate of 2 °C min^{-1} as shown by the TGA curves in Fig. S4. Elemental red phosphorus is expected to sublime around 400 °C and loses a considerable weight (~90%) before reaching 500 °C [81]. However, no weight loss was observed in the VP_2 powder across the temperature range, indicating

absence of any residual elemental phosphorus. The crystallographic and chemical results mentioned above clearly evince the successful preparation of polycrystalline VP_2 consisting of P and V oxides on the surface, with no residual elemental phosphorous.

To investigate the electrochemical performance of VP_2, galvanostatic charge-discharge tests were performed on a half-cell configuration consisting a Na metal counter electrode and Na[FSA]–[C_3C_1pyrr][FSA] (20 : 80 in mol) ionic liquid IL in the voltage range of 0.005–2.0 V at temperatures of 25 and 90 °C as highlighted in Fig. 3. The electrode was prepared in the weight ratio (wt%) of VP_2:AB:PAI = 75:15:10. The current density was set to 100 mA $g^{-1}$and charge-discharge curves were obtained from the first three cycles measured at temperatures of 25 and 90 °C as shown in Fig. 3a and b, respectively (see Fig. S5 for corresponding (dQ/dV) plots obtained at 90 °C). During the initial cycle performed at 25 °C, a relatively low discharge capacity of 49 mAh g^{-1} corresponding to a Coulombic efficiency of 37% was observed. However, at 90 °C, a significant improvement was observed where an initial discharge capacity of 243 mAh g^{-1} along with an improved Coulombic efficiency of 53% were attained. High reversibility was also observed in subsequent second and third cycles for both temperatures. To assess the rate capability of the electrode, charge-discharge measurements under varying current densities ranging from 100 to 8000 mA g^{-1} (five cycles per current density) were taken at 90 °C. The electrode material is found to facilitate a stable capacity at each current rate, showing discharge capacities of 241, 212, and 131 mAh g^{-1} at current densities of 100, 1000, and 8000 mA g^{-1}, respectively (Fig. 3c). A high recuperation was also noted after the rate test at 8000 mA g^{-1}. Charge-discharge curves from the last cycle of each current density were thereafter collected as shown in Fig. 3d. The slope gradient and the polarization of the discharge curves are seen to increase with increasing current density. The cycle performance of the VP_2 electrode was thereafter evaluated at a current density of 500

mA g^{-1} for 500 cycles at temperatures of 25 and 90 °C as highlighted in Fig. 3e. The first three cycles were performed at a current rate of 100 mA g^{-1} for activation. At 90 °C, a high capacity retention of 102.4 % along with a Coulombic efficiency of 99.92 % were attained at the 500^{th} cycle *vis à vis* the 4th cycle (discharge capacity = 207 mAh g^{-1}). The slight increase in discharge capacity noted after cycling can be attributed to the activation of the electrode achieved after raising the current density from 100 to 500 mA g^{-1}. This is congruent with observations made on copper-phosphide carbon composite electrode in a previous study [82]. On the other hand, at 25 °C, a rather poor capacity of 24 mAh g^{-1} was achieved the 500^{th} cycle, even though slight increases were noted throughout the cycles. These results demonstrate significant improvements in the performance of the VP_2 electrode in the IL electrolyte during operations at intermediate temperatures of 90 °C. It was also found that adjusting the amount of AB in the electrode influences the irreversible capacity. Therefore, to confirm the effect of AB on the electrochemical behavior of the electrode, a control experiment was performed using a VP_2 electrode containing a lower AB weight ratio (wt%) of VP_2:AB:PAI = 90:5:5. A higher first and second cycle Coulombic efficiency (67.7 % and 95.8 %, respectively) is achieved by VP_2:AB:PAI = 90:5:5 in comparison with that of VP_2:AB:PAI = 75:15:5 (53.2 % and 94.2 %, respectively). This can be ascribed to reduced electrolyte decomposition as a result of the low specific surface area achieved by decreasing the amount of AB in the electrode (Fig. S6 and Fig. 3b) [83]. It should be noticed that the discharge capacity in the first cycle is similar in the both the cases (249 mAh g^{-1} and 243 mAh g^{-1} for 5 wt% and 15 wt% AB in the electrode, respectively). However, the discharge capacity of the electrode with less AB gradually decreases over the 500 cycles, providing a low capacity retention of 39.2%, which suggests that the cyclability of the VP_2 electrode deteriorates with reduction in the amount of conductive AB.

To assess the electrochemical behavior of the electrode without being influenced by the counter electrode material, electrochemical impedance spectroscopy (EIS) using symmetric cells is generally employed in various battery systems [84, 85], including sodium secondary batteries [86]. Fig. 4 shows the Nyquist plot of a VP_2/VP_2 symmetric cell obtained by EIS at 25, 60 and 90 °C. To prepare the VP_2 electrode for the symmetric cell EIS test, the Na/IL/VP_2 half cells were charged to 0.5 V. The semicircle appearing at a frequency range of 1–200 Hz corresponds to the charge-transfer resistance whereas the intercept to the horizontal axis in the high frequency region corresponds to the bulk resistance. It is apparent that both the charge-transfer and bulk resistances decrease with increase in temperature, as shown in Fig. 4a and the fitted EIS parameters shown in Table S1. The equivalent circuit reflected in Fig. 4c was used for fitting the curves of the Nyquist plot provided in Figs. 4a and 4b. This finding was further supported by EIS tests of the Na/VP_2 half-cell during 500 cycles at 90 °C (the cycling conditions were the same as those in the case of Fig. 3e). The impedance spectra were measured at a cell voltage of 0.5 V during the charging step at the 2nd, 4th, 11th, 51st, 101st, and 501st cycles. The Nyquist plots show one depressed semicircle which is composed of two semicircles at high frequency ($R_2 \approx 10^4$ Hz) and medium frequency ($R_3 \approx 10^2$ Hz) (see Table S2 for the fitted EIS parameters). Although the medium-frequency component is unambiguously assignable to the charge-transfer resistance, there has been no conclusive assignment of the high-frequency component [86, 87]. Nevertheless, the resistances of both the medium- and high-frequency components (R_2 and R_3) decrease progressively with cycling, indicating an overall decrease in interfacial resistance upon successive cycling.

To draw a comparison between the electrochemical performance of VP_2 electrode in IL and other commonly used electrolytes, charge-discharge and cyclability tests were performed using 1 M $NaPF_6$ in an EC:DEC (1:1 v/v) organic electrolyte in the voltage range of 0.005–2.0 V at 25 °C

as shown in Fig. S7. During the initial cycle, the organic electrolyte was found to yield higher charge and discharge capacities (289 and 148 mAh g^{-1}, respectively) in contrast to the charge and discharge capacities (134 mAh g^{-1} and 49 mAh g^{-1}, respectively) obtained from IL at the same temperature (Figs. S7a and 3a). The cycle performance of the electrode was thereafter examined at a current rate of 500 mA g^{-1} (with first three cycles performed at 100 mA g^{-1} for activation) for 500 cycles at 25 °C. As shown in Fig. S7b, the VP_2 electrode in the organic electrolyte exhibited a progressive capacity fading throughout the cycles, achieving a discharge capacity of 17 mAh g^{-1} at the 500^{th} cycle. As additives such as fluoroethylene carbonate (FEC) have been known to improve the functionality sodium metal counter electrode and enhance cell performance among NIBs [88], electrochemical performance of the VP_2 electrode was evaluated using 1 M $NaPF_6$ in EC:DEC (1:1 v/v) with 3 wt% FEC as shown in Fig. S7c and d. The initial charge and discharge capacities (295 and 141 mAh g^{-1}, respectively) obtained are essentially similar to those from the electrolyte with no additive. Moreover, high capacity degradation is observed throughout the 500 cycles as portrayed by the cyclability results (Fig. S7d). Fig. S8 shows the (a,b) charge-discharge curves and (c) cycle performance of the VP_2 electrode measured with 1 M $NaPF_6$ in EC:DEC (1:1 v/v) with 3 wt% FEC and IL electrolyte at 60 °C, respectively. The current density was 100 mA g^{-1} for 1–3 cycles and 500 mA g^{-1} 4–50 and the cut-off voltage was 0.005–2.0 V. The reversible capacity and Coulombic efficiency obtained in the first cycle improved significantly in both the cases (199 mAh g^{-1} and 48.4 % for organic electrolyte and 215 mAh g^{-1} and 65.6 % for IL electrolyte) as compared to those at 25 °C. In the cycle test, VP_2 with IL electrolyte displayed 100% capacity retention after 50 cycles with 99.8 % Coulombic efficiency, whereas severe capacity fading was observed with organic electrolyte in the first 10 cycles only. These results not only evinced the incompatibility of VP_2 with organic electrolyte but also emphasize on the importance

of intermediate temperatures in enhancing the performance of ionic liquid electrolyte.

During battery operations, the properties of the SEI layer formed on the surface of the negative electrode have been found to significantly influence critical parameters such as initial Coulombic efficiency, rate capability, and cyclability among full cells [89]. As such, SEM and XPS analyses were employed to examine the surface properties of the VP_2 electrode after electrochemical operations. As illustrated by Fig. 5, the SEM image of the pristine electrode displays an even distribution of VP_2 particles with a mean diameter of a few micrometers in the composite electrode (Fig. 5a). However, after 500 cycles, the electrode surface was found to be coated in a uniform and partially porous SEI layer with no visible cracks (Fig. 5b). Thereafter, P 2p and V 2p XPS spectra of the VP_2 electrode were taken at different etching times (0, 30, 60 and 120 s) after the initial charging phase at the cut-off voltage of 2.0 V as shown in Fig. S10. No signals corresponding to P and V were detected at 0s. However, just after 30s of Ar-ion bombardment, all peaks assignable to P−O and V−P were visible. Further etching resulted in no change in this observation. The VP_2/VP_2 symmetric cell EIS was measured with 1 M $NaPF_6$ in EC:DEC (1:1 v/v) with 3 wt% FEC and IL electrolytes at 25 °C. The Na/VP_2 half-cells were disassembled after charging up to 0.5 V during the 2nd cycle at 10 mA g^{-1}. The Nyquist plots in Fig. S9a shows considerably large SEI layer resistance (R_2) and charge transfer resistance (R_3) in the case of organic electrolyte (R_2 = 65.34 ohm and R_3 = 337.8 ohm; listed in Table S3) as compared to that in IL electrolyte (R_2 = 4.21 ohm and R_3 = 19.49 ohm), indicating improved interfacial properties of the SEI layer formed in the IL electrolyte. These results not only confirm the presence of the SEI layer as demonstrated by the SEM analysis, but also indicate the tenuity of the SEI layer in the VP_2 electrode.

The charge and discharge mechanism of VP_2 was investigated using *ex-situ* XRD, XAFS,

and MAS NMR spectroscopy, for the sample charged and discharged at 90 °C under the following current densities: 10 and 100 mA g^{-1} for XRD and 100 mA g^{-1} for XAFS and MAS NMR). Fig. 6 shows the XRD patterns of the pristine, charged (0.005 V), and discharged (2.0 V) VP_2 electrode, taken at current density of 10 and 100 mA g^{-1}. In Fig. 6a, a strong intensity peak of Na_3P appears at 36.12° after charging. However, other peaks corresponding to VP_2 remain essentially intact, indicating that only some parts of VP_2 took part in the conversion-based mechanism while a majority remained inactive at 10 mA g^{-1}. During the discharge process, the Na_3P Bragg peak disappears indicating the reversibility of the conversion reaction. In Fig. 6b, all the diffraction peaks in the XRD patterns are indexable to VP_2 phase in any state and remained unchanged during charging and discharging at 100 mA g^{-1}. To ascertain the electronic structural changes in VP_2 during charging and discharging process, X-ray absorption spectroscopy (XAS) was conducted. Fig. 7 shows the V *K*-edge X-ray absorption near-edge structure (XANES) spectra and the corresponding Fourier transforms of the extended X-ray absorption fine structure (EXAFS) oscillations for the pristine, charged (0.005 V) and discharged (2.0 V) VP_2 electrode. The V *K*-edge XANES data show insignificant electronic structural changes after charge and discharge compared to the pristine state. Moreover, the EXAFS peaks in the pristine state (2.02, 2.74 and 3.41 Å) overlap with the ones in the charged (2.02, 2.76 and 3.40 Å) and discharged states (2.02, 2.76 and 3.43 Å), indicating negligible change in the V−P bond length (without V metal formation) as observed in the aforementioned XRD results. The small change observed in V *K*-edge XANES is congruent to the lithiation of VP_2 [44]. This reaction mechanism was further investigated by MAS NMR for the pristine, charged (0.005 V) and discharged (2.0 V) VP_2 electrodes. Fig. 8a shows the NMR spectra obtained. In the pristine state, the multiple peaks appearing in a broad range of 300–900 ppm are assignable to VP_2, judging from their similarity to those observed in a

comprehensive ^{31}P MAS NMR study done performed for transition metal phosphides.[90] After charging, a small peak at −208.7 ppm appears, which is clearly assigned to Na_3P as reported in several studies [91, 92]. The Na_3P peak disappears after charging, indicating the reversibility in reaction. The aforementioned results suggest a reversible conversion-based mechanism of VP_2 at 90 °C forming Na_3P after discharging. However, the lower reversible capacity (243 mAh g^{-1} at 90 °C) compared to the theoretical capacity of 1312 mAh g^{-1} suggests that the conversion reaction only partially occurs and the resulting VP_{2-x} becomes inert against the conversion reaction when x reaches ~0.37. This x value represents the number of moles of phosphorus in VP_2 participating in the conversion reaction and is calculated by dividing the practical capacity (243 mAh g^{-1}) by the theoretical value (1312 mAh g^{-1}) and multiplying the resulting value by two. Fig. 8b shows the schematic illustration of this mechanism. It should be noted that good cyclability was achieved through conversion reaction, when a composite electrode with an AB loading of 15 wt% was used, whereas capacity fading was observed in a composite electrode with a 5 wt% loading of AB (see Fig. S6b). These observations suggest that carbon (AB) plays an important role in buffering the large volume change and maintaining the electrical contact between active material during cycling.

Conclusions

In this study, we report the electrochemical performance and reaction mechanism of VP_2 as a negative electrode material for NIBs using the Na[FSA]–[C_3C_1pyrr][FSA] IL electrolyte. The VP_2 active material was prepared via a one-step high energy ball-milling process 850 rpm for 20 h. XRD, SEM, TEM, and XPS analyses were used to characterize the VP_2 as a polycrystalline material with a uniform distribution of V and P throughout the crystallite. Galvanostatic tests performed on the electrode in the IL at 25 and 90 °C obtained discharge capacities of 49 mAh g^{-1}

(Coulombic efficiency of 37%) and 243 mAh g^{-1} (Coulombic efficiency of 53%) during the initial cycles examined at 25 and 90 °C, respectively. The cycle and rate performance tests further revealed a high capacity retention of 102.4% after 500 cycles with a discharge capacity of 131 mAh g^{-1} achieved at 8000 mA g^{-1} at 90 °C, indicating enhanced performance at intermediate temperatures. The EIS test conducted using a symmetric VP_2/VP_2 cell manifested a significant decrease in charge transfer resistance with increasing operating temperatures. The interfacial resistance of the Na/VP_2 half-cell was also observed to steadily decrease with progressive cycling at 90 °C, pointing towards the formation of a uniform and thin SEI layer. This was further corroborated by SEM and XPS depth profiles which also affirmed the rate capability and good cyclability results previously attained. Ex-situ XRD and MAS NMR spectroscopy revealed that VP_2 underwent a conversion-type mechanism to form Na_3P after charging. However, a significant part of VP_2 remained inactive. It is worthy to note that the XAFS measurements could not discern the phosphorus redox reactions.

Acknowledgements

This study was supported by the Japanese Ministry of Education, Culture, Sports, Science, and Technology (MEXT) program Elements Strategy Initiative to Form Core Research Center (JPMXP0112101003).

References

[1] V. Khare, S. Nema, P. Baredar, Renew. Sust. Energy Rev., 58 (2016) 23-33.

[2] M. Yekini Suberu, M. Wazir Mustafa, N. Bashir, Renew. Sust. Energy Rev., 35 (2014) 499-514.

[3] J.M. Tarascon, M. Armand, Nature, 414 (2001) 359-367.

[4] M.S. Whittingham, Chem. Rev., 104 (2004) 4271-4302.

[5] Y.J. Lee, H. Yi, W.-J. Kim, K. Kang, D.S. Yun, M.S. Strano, G. Ceder, A.M. Belcher, Science, 324 (2009) 1051-1055.

[6] M. Wentker, M. Greenwood, J. Leker, Energies, 12 (2019) 504.

[7] F. Li, Z. Wei, A. Manthiram, Y. Feng, J. Ma, L. Mai, J. Mater. Chem. A, 7 (2019) 9406-9431.

[8] L.P. Wang, L. Yu, X. Wang, M. Srinivasan, Z.J. Xu, J. Mater. Chem. A, 3 (2015) 9353-9378.

[9] A. Ponrouch, D. Monti, A. Boschin, B. Steen, P. Johansson, M.R. Palacín, J. Mater. Chem. A, 3 (2015) 22-42.

[10] J.-Y. Hwang, S.-T. Myung, Y.-K. Sun, Chem. Soc. Rev., 46 (2017) 3529-3614.

[11] M.D. Slater, D. Kim, E. Lee, C.S. Johnson, Adv. Funct. Mater., 23 (2013) 947-958.

[12] B.L. Ellis, L.F. Nazar, Curr. Opin. Solid State Mater. Sci., 16 (2012) 168-177.

[13] N. Yabuuchi, K. Kubota, M. Dahbi, S. Komaba, Chem. Rev., 114 (2014) 11636-11682.

[14] S.-W. Kim, D.-H. Seo, X. Ma, G. Ceder, K. Kang, Adv. Energy Mater., 2 (2012) 710-721.

[15] U.S.G. Survey, Mineral Commodity Summaries 2019, Soda Ash, (2019) 154.

[16] Y. Nozaki, EOS. Trans, 78 (1997) 221.

[17] H. Zhang, Y. Huang, H. Ming, G. Cao, W. Zhang, J. Ming, R. Chen, J. Mater. Chem. A, 8 (2020) 1604-1630.

[18] J. Mao, T. Zhou, Y. Zheng, H. Gao, H.k. Liu, Z. Guo, J. Mater. Chem. A, 6 (2018) 3284-3303.

[19] W. Li, M. Li, K.R. Adair, X. Sun, Y. Yu, J. Mater. Chem. A, 5 (2017) 13882-13906.

[20] H. Pan, Y.-S. Hu, L. Chen, Energy Environ. Sci., 6 (2013) 2338-2360.

[21] D.A. Stevens, J.R. Dahn, J. Electrochem. Soc., 147 (2000) 1271.

[22] M. Goktas, C. Bolli, E.J. Berg, P. Novák, K. Pollok, F. Langenhorst, M.v. Roeder, O. Lenchuk, D. Mollenhauer, P. Adelhelm, Adv. Energy Mater., 8 (2018) 1702724.

[23] Y. Wen, K. He, Y. Zhu, F. Han, Y. Xu, I. Matsuda, Y. Ishii, J. Cumings, C. Wang, Nat. Commun., 5 (2014) 4033.

[24] B. Xiao, T. Rojo, X. Li, ChemSusChem, 12 (2019) 133-144.

[25] M. Dahbi, M. Kiso, K. Kubota, T. Horiba, T. Chafik, K. Hida, T. Matsuyama, S. Komaba, J. Mater. Chem. A, 5 (2017) 9917-9928.

[26] A.C.S. Jensen, E. Olsson, H. Au, H. Alptekin, Z. Yang, S. Cottrell, K. Yokoyama, Q. Cai, M.-M. Titirici, A.J. Drew, J. Mater. Chem. A, 8 (2020) 743-749.

[27] N. Sun, H. Liu, B. Xu, J. Mater. Chem. A, 3 (2015) 20560-20566.

[28] A. Rudola, K. Saravanan, S. Devaraj, H. Gong, P. Balaya, Chem. Commun., 49 (2013) 7451-7453.

[29] A. Rudola, N. Sharma, P. Balaya, Electrochem. Commun., 61 (2015) 10-13.

[30] A. Rudola, K. Saravanan, C.W. Mason, P. Balaya, J. Mater. Chem. A, 1 (2013) 2653-2662.

[31] S. Fang, D. Bresser, S. Passerini, Adv. Energy Mater., 10 (2020) 1902485.

[32] D. Deng, M.G. Kim, J.Y. Lee, J. Cho, Energy Environ. Sci., 2 (2009) 818-837.

[33] L. Wu, D. Bresser, D. Buchholz, G.A. Giffin, C.R. Castro, A. Ochel, S. Passerini, Adv. Energy Mater., 5 (2015) 1401142.

[34] F. Klein, R. Pinedo, P. Hering, A. Polity, J. Janek, P. Adelhelm, J. Phys. Chem. C, 120 (2016) 1400-1414.

[35] Q. Xia, W. Li, Z. Miao, S. Chou, H. Liu, Nano Res., 10 (2017) 4055-4081.

[36] L. Liu, Q. Li, Z. Wang, J. Yan, Y. Chen, Funct. Mater. Lett., 11 (2018) 1830001.

[37] Z. Li, H. Zhao, J. Mater. Chem. A, 6 (2018) 24013-24030.

[38] Y. Kim, Y. Kim, A. Choi, S. Woo, D. Mok, N.-S. Choi, Y.S. Jung, J.H. Ryu, S.M. Oh, K.T. Lee, Adv. Mater., 26 (2014) 4139-4144.

[39] S.-O. Kim, A. Manthiram, Chem. Commun., 52 (2016) 4337-4340.

[40] G. Chang, Y. Zhao, L. Dong, D.P. Wilkinson, L. Zhang, Q. Shao, W. Yan, X. Sun, J. Zhang, J. Mater. Chem. A, 8 (2020) 4996-5048.

[41] Y. Fu, Q. Wei, G. Zhang, S. Sun, Adv. Energy Mater., 8 (2018) 1703058.

[42] C.-M. Park, Y.-U. Kim, H.-J. Sohn, Chem. Mater., 21 (2009) 5566-5568.

[43] Y.-U. Kim, B.W. Cho, H.-J. Sohn, J. Electrochem. Soc., 152 (2005) A1475-A1478.

[44] F. Gillot, M. Ménétrier, E. Bekaert, L. Dupont, M. Morcrette, L. Monconduit, J.M. Tarascon, J. Power Sources, 172 (2007) 877-885.

[45] K.-H. Kim, J. Choi, S.-H. Hong, Chem. Commun., 55 (2019) 3207-3210.

[46] K.-H. Kim, C.-H. Jung, W.-S. Kim, S.-H. Hong, J. Power Sources, 400 (2018) 204-211.

[47] K. Xu, Chem. Rev., 114 (2014) 11503-11618.

[48] G.G. Eshetu, S. Grugeon, S. Laruelle, S. Boyanov, A. Lecocq, J.-P. Bertrand, G. Marlair, Phys. Chem. Chem. Phys., 15 (2013) 9145-9155.

[49] K. Matsumoto, Y. Okamoto, T. Nohira, R. Hagiwara, J. Phys. Chem. C, 119 (2015) 7648-7655.

[50] M. Galiński, A. Lewandowski, I. Stępniak, Electrochim. Acta, 51 (2006) 5567-5580.

[51] I. Osada, H. de Vries, B. Scrosati, S. Passerini, Angew. Chem. Int. Ed., 55 (2016) 500-513.

[52] A. Fernicola, F. Croce, B. Scrosati, T. Watanabe, H. Ohno, J. Power Sources, 174 (2007) 342-348.

[53] D. Monti, E. Jónsson, M.R. Palacín, P. Johansson, J. Power Sources, 245 (2014) 630-636.

[54] D.R. MacFarlane, N. Tachikawa, M. Forsyth, J.M. Pringle, P.C. Howlett, G.D. Elliott, J.H. Davis, M. Watanabe, P. Simon, C.A. Angell, Energy Environ. Sci., 7 (2014) 232-250.

[55] K. Matsumoto, J. Hwang, S. Kaushik, C.-Y. Chen, R. Hagiwara, Energy Environ. Sci., 12 (2019) 3247-3287.

[56] A. Basile, M. Hilder, F. Makhlooghiazad, C. Pozo-Gonzalo, D.R. MacFarlane, P.C. Howlett, M. Forsyth, Adv. Energy Mater., 8 (2018) 1703491.

[57] L.G. Chagas, D. Buchholz, L. Wu, B. Vortmann, S. Passerini, J. Power Sources, 247 (2014) 377-383.

[58] N. Wongittharom, T.-C. Lee, C.-H. Wang, Y.-C. Wang, J.-K. Chang, J. Mater. Chem. A, 2 (2014) 5655-5661.

[59] S.A. Mohd Noor, P.C. Howlett, D.R. MacFarlane, M. Forsyth, Electrochim. Acta, 114 (2013) 766-771.

[60] C. Ding, T. Nohira, R. Hagiwara, K. Matsumoto, Y. Okamoto, A. Fukunaga, S. Sakai, K. Nitta, S. Inazawa, J. Power Sources, 269 (2014) 124-128.

[61] H. Usui, Y. Domi, M. Shimizu, A. Imoto, K. Yamaguchi, H. Sakaguchi, J. Power Sources, 329 (2016) 428-431.

[62] L. Wu, A. Moretti, D. Buchholz, S. Passerini, D. Bresser, Electrochim. Acta, 203 (2016) 109-116.

[63] K. Matsumoto, C.Y. Chen, T. Kiko, J. Hwang, T. Hosokawa, T. Nohira, R. Hagiwara, ECS Trans., 75 (2016) 139-145.

[64] T. Yamamoto, T. Nohira, R. Hagiwara, A. Fukunaga, S. Sakai, K. Nitta, Electrochim. Acta, 193 (2016) 275-283.

[65] J. Hwang, K. Matsumoto, R. Hagiwara, Adv. Sustainable Syst., 2 (2018) 1700171.

[66] M. Forsyth, H. Yoon, F. Chen, H. Zhu, D.R. MacFarlane, M. Armand, P.C. Howlett, J. Phys. Chem. C, 120 (2016) 4276-4286.

[67] A. Fukunaga, T. Nohira, R. Hagiwara, K. Numata, E. Itani, S. Sakai, K. Nitta, S. Inazawa, J. Power Sources, 246 (2014) 387-391.

[68] H. Usui, Y. Domi, K. Fujiwara, M. Shimizu, T. Yamamoto, T. Nohira, R. Hagiwara, H. Sakaguchi, ACS Energy Lett., 2 (2017) 1139-1143.

[69] S. Kaushik, J. Hwang, K. Matsumoto, Y. Sato, R. Hagiwara, ChemElectroChem, 5 (2018) 1340-1344.

[70] C. Ding, T. Nohira, R. Hagiwara, J. Power Sources, 388 (2018) 19-24.

[71] M. Dahbi, M. Fukunishi, T. Horiba, N. Yabuuchi, S. Yasuno, S. Komaba, J. Power Sources, 363 (2017) 404-412.

[72] C.-H. Wang, C.-H. Yang, J.-K. Chang, Chem. Commun., 52 (2016) 10890-10893.

[73] S. Kaushik, K. Matsumoto, Y. Sato, R. Hagiwara, Electrochem. Commun., 102 (2019) 46-51.

[74] W. Jeitschko, P.C. Donohue, V. Johnson, Acta Crystallogr. Sect. B, 32 (1976) 1499-1505.

[75] M. Geolin, B. Carlsson, S. Rundqvist, Acta Chem. Scand. A, 29 (1975) 706-708.

[76] K. Selte, A. Kjekshus, A.F. Andresen, Acta Chem. Scand., 26 (1972) 4057-4062.

[77] J.-h. Yang, S.-h. Cheng, X. Wang, Z. Zhang, X.-r. Liu, G.-h. Tang, Trans. Nonferrous Met. Soc. China, 16 (2006) s796-s803.

[78] C.E. Myers, H.F. Franzen, J.W. Anderegg, Inorg. Chem., 24 (1985) 1822-1824.

[79] H. Igarashi, K. Tsuji, T. Okuhara, M. Misono, J. Phys. Chem., 97 (1993) 7065-7071.

[80] P. Mezentzeff, Y. Lifshitz, J.W. Rabalais, Nucl. Instrum. Meth. B, 44 (1990) 296-301.

[81] J. Smajic, A. Alazmi, S.P. Patole, Pedro M.F.J. Costa, RSC Adv., 7 (2017) 39997-40004.

[82] S. Kaushik, K. Matsumoto, Y. Sato, R. Hagiwara, ChemElectroChem, 7 (2020) 2477-2484.

[83] L. Fransson, T. Eriksson, K. Edström, T. Gustafsson, J.O. Thomas, J. Power Sources, 101 (2001) 1-9.

[84] C.H. Chen, J. Liu, K. Amine, J. Power Sources, 96 (2001) 321-328.

[85] N. Ogihara, Y. Itou, T. Sasaki, Y. Takeuchi, J. Phys. Chem. C, 119 (2015) 4612-4619.

[86] J. Hwang, K. Matsumoto, R. Hagiwara, J. Phys. Chem. C, 122 (2018) 26857-26864.

[87] S.S. Zhang, K. Xu, T.R. Jow, Electrochim. Acta, 51 (2006) 1636-1640.

[88] J. Hwang, K. Takeuchi, K. Matsumoto, R. Hagiwara, J. Mater. Chem. A, 7 (2019) 27057-27065.

[89] L. Ji, M. Gu, Y. Shao, X. Li, M.H. Engelhard, B.W. Arey, W. Wang, Z. Nie, J. Xiao, C. Wang, J.-G. Zhang, J. Liu, Adv. Mater., 26 (2014) 2901-2908.

[90] E. Bekaert, J. Bernardi, S. Boyanov, L. Monconduit, M.L. Doublet, M. Ménétrier, J. Phys. Chem. C, 112 (2008) 20481-20490.

[91] R. Morita, K. Gotoh, M. Dahbi, K. Kubota, S. Komaba, K. Tokiwa, S. Arabnejad, K. Yamashita, K. Deguchi, S. Ohki, T. Shimizu, R. Laskowski, H. Ishida, J. Power Sources, 413 (2019) 418-424.

[92] L.E. Marbella, M.L. Evans, M.F. Groh, J. Nelson, K.J. Griffith, A.J. Morris, C.P. Grey, J. Am. Chem. Soc., 140 (2018) 7994-8004.

Tables and Figures

Table 1 Summary of ball-milling conditions and electrochemical performance of V_xP_y compounds for NIBs and LIBs

V_xP_y/Li or Na	Ball-milling conditions				Electrochemical performance[a]	
	Speed (rpm)	Time (h)	Ball: powder ratio (w/w)	Crystal system (space group)	1st cycle discharge capacity (mAh g^{-1}) / rate (mA g^{-1})	Electrolyte
VP/Li [42]	unknown	6	20:1	hexagonal ($P6_3/mnc$)	291/100	$LiPF_6$ in EC/DEC
$VP_{1.75}$@C/Li [46]	300	60	20:1	tetragonal ($P\bar{4}m2$)	882/100	$LiPF_6$ in EC/DMC
$VP_{1.75}$/Na [45]	300	60	20:1	tetragonal ($P\bar{4}m2$)	240/50	$NaClO_4$ in EC/DMC with 5 vol% FEC
$VP_{1.75}$-1.25P/Na [73]	400	20	50:1	tetragonal ($P\bar{4}m2$)	560/100 740/100*	Na[FSA]-$[C_3C_1pyrr][FSA]$ (2:8 mol ratio)
VP_2/Li [44]	600	50	10:1	monoclinic ($C2/m$)	890/100	$LiPF_6$ in EC/DMC
VP_2/Na (this work)	850	20	50:1	monoclinic ($C2/m$)	49/100 243/100*	Na[FSA]-$[C_3C_1pyrr][FSA]$ (2:8 mol ratio)
VP_4/Li [43]	-	48	20:1	monoclinic ($C2/c$)	1290/-	$LiPF_6$ in EC/DEC

[a]Temperature is 25°C unless specified with asterisk (90 °C for the one with asterisk)
[b]Molar concentration of electrolyte = 1 M unless specified; ratio of solvents = 1:1 v/v unless specified

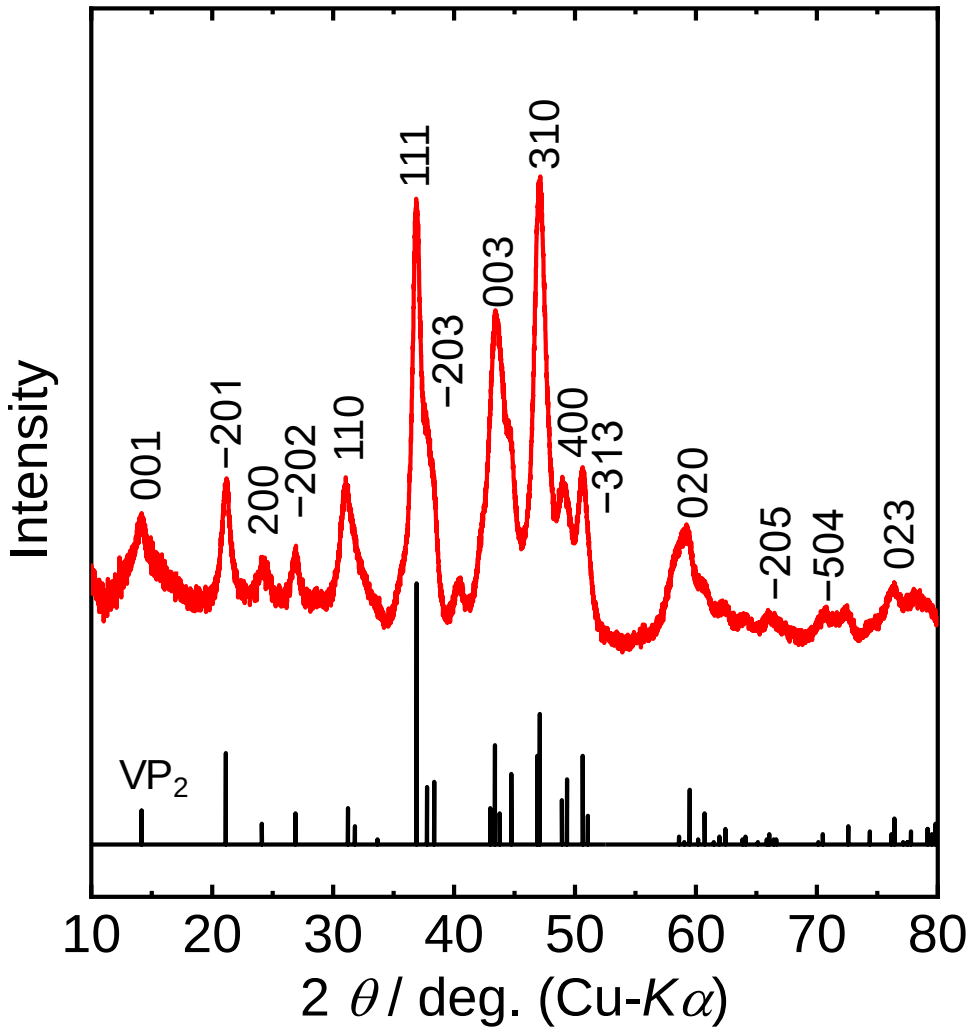

Fig. 1 The XRD pattern of the pristine VP_2 powder prepared by HEBM. The reference pattern of VP_2 is also shown for comparison [75].

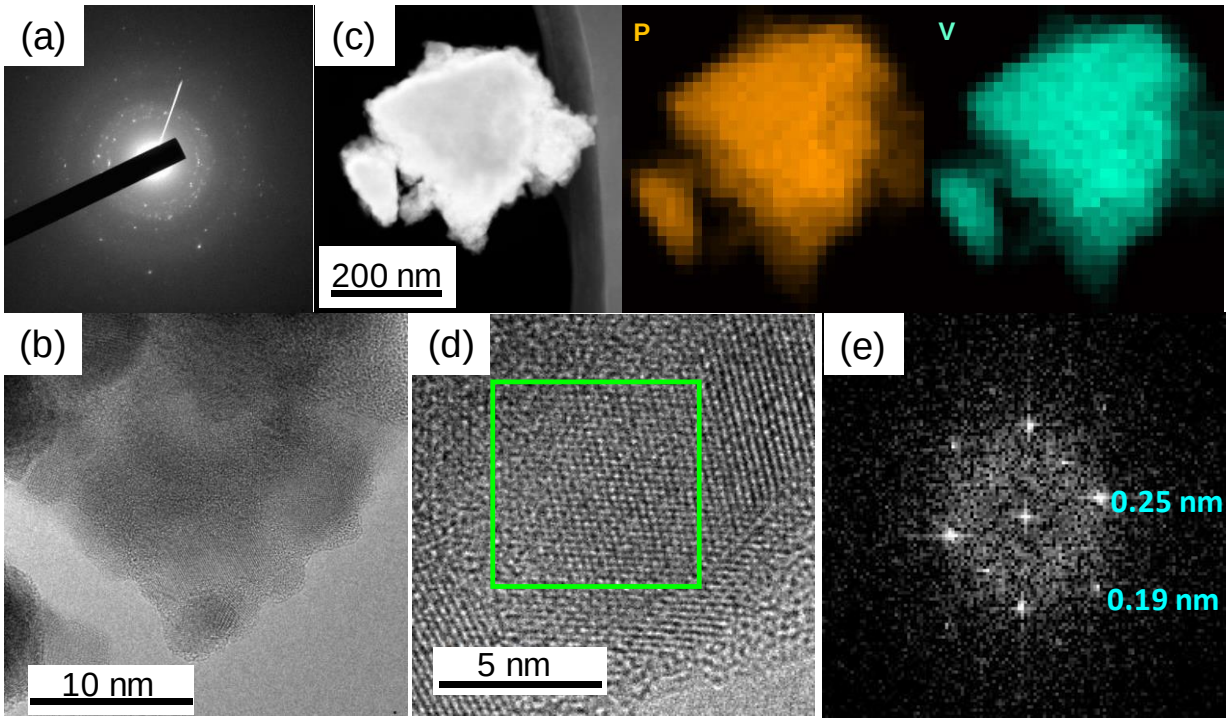

Fig. 2 (a) SAED pattern, (b) HRTEM image, (c) STEM-EDX mapping, (d) magnified HRTEM image, and (e) FFT power spectrum of the pristine VP_2 powder.

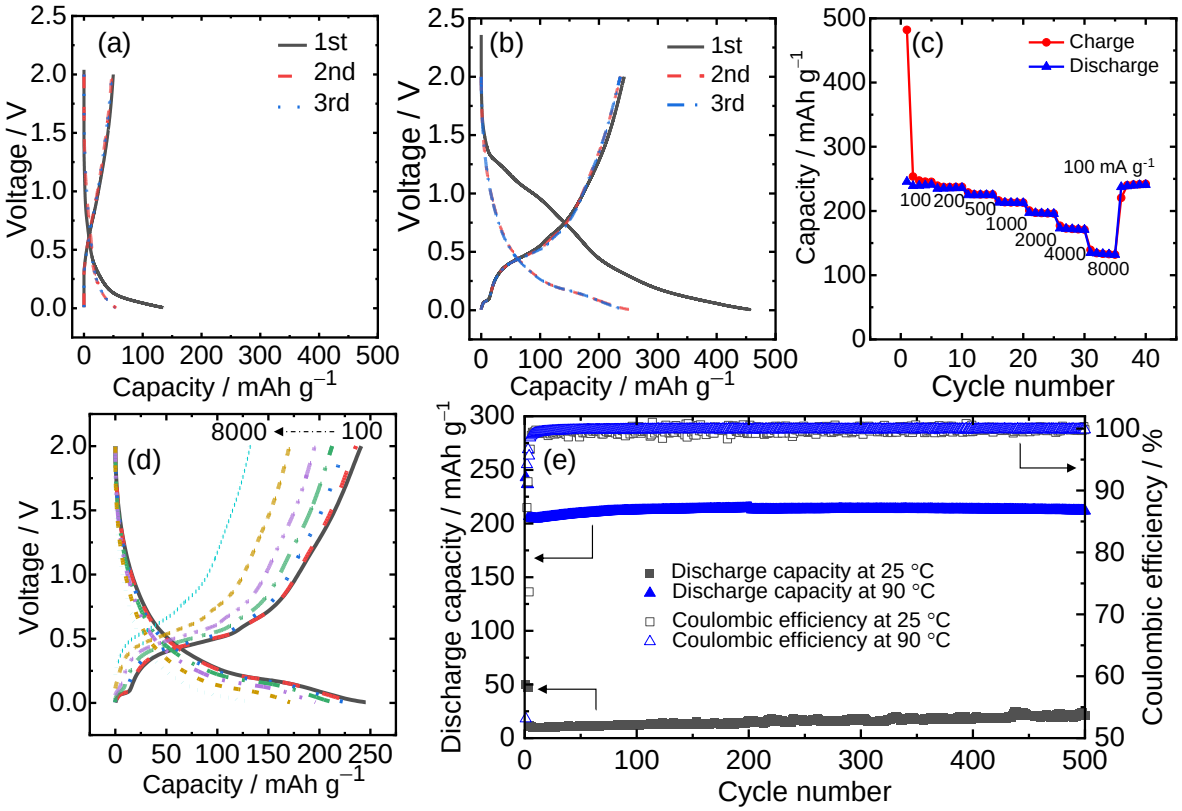

Fig. 3 Electrochemical behavior of VP_2 in a Na/VP_2 coin-type cell with the IL electrolyte (cut-off voltage: 0.005–2.0 V and counter electrode: Na metal disc). Galvanostatic charge-discharge curves for the first three cycles at (a) 25 and (b) 90 °C (current density: 100 mAg^{-1}). (c) Rate capability at 90 °C (current density: 100–8000 mAg^{-1}) and (d) galvanostatic charge-discharge curves of the last cycle for each rate. (e) Cycleability for 500 cycles at 25 and 90 °C (rate: 100 mAg^{-1} for the first three cycles to activate the electrode and 500 mA g^{-1} for the rest of cycles).

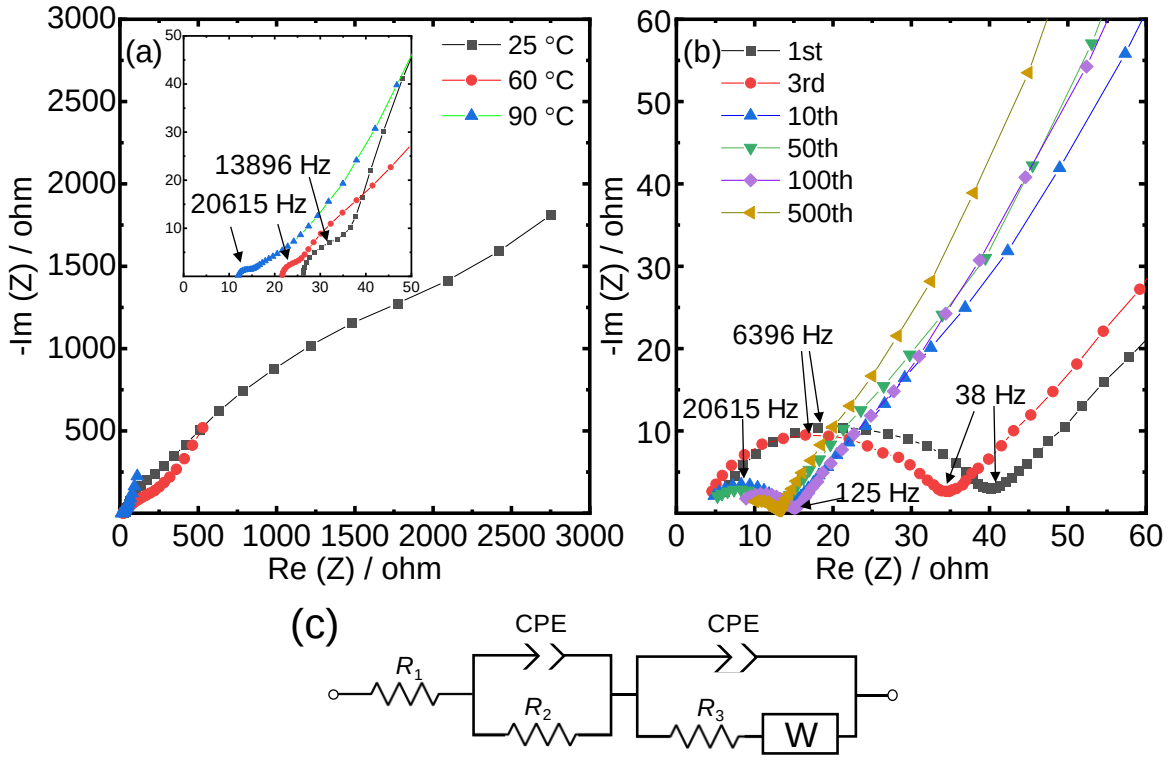

Fig. 4 (a) Nyquist plots of the VP_2/VP_2 symmetric cell using the IL electrolyte at 25, 60, and 90 °C. The electrodes were charged in the Na/IL/VP_2 half-cell configuration to the cell voltage of 0.5 V and retrieved to prepare the symmetric cells. Inset shows the magnified view of the plots. (b) Nyquist plot of the Na/VP_2 half-cell using the IL electrolyte during 500 cycles at 90 °C. (c) Equivalent circuit for fitting Nyquist plots in both symmetric cell and half-cell cases. All the EIS tests were performed with an amplitude of 20 mV and frequency range of 100 kHz−10mHz.

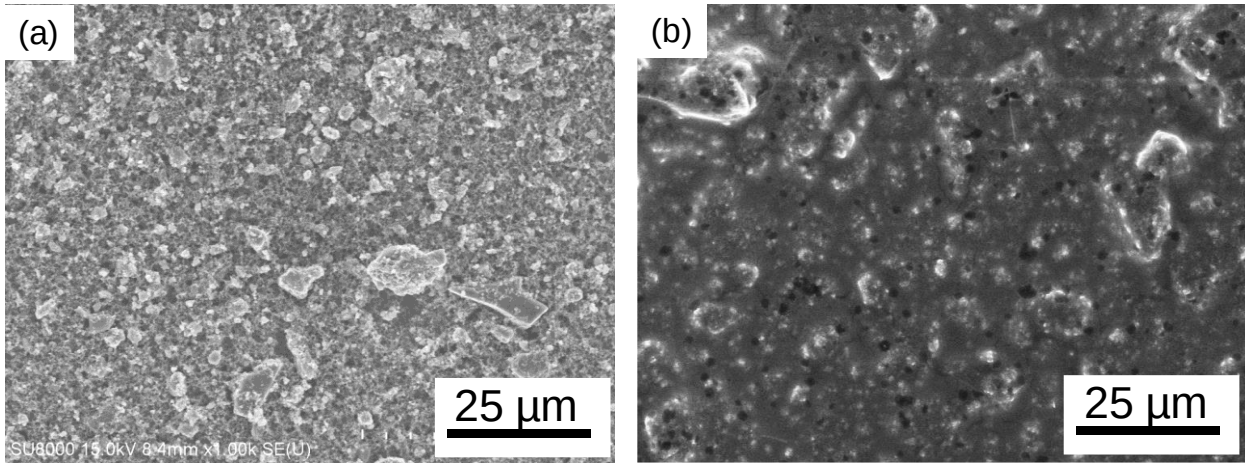

Fig. 5 SEM images of the VP_2 electrode before and after cycling. (a) pristine electrode and (b) after 500 cycles at 90 °C using the IL electrolyte.

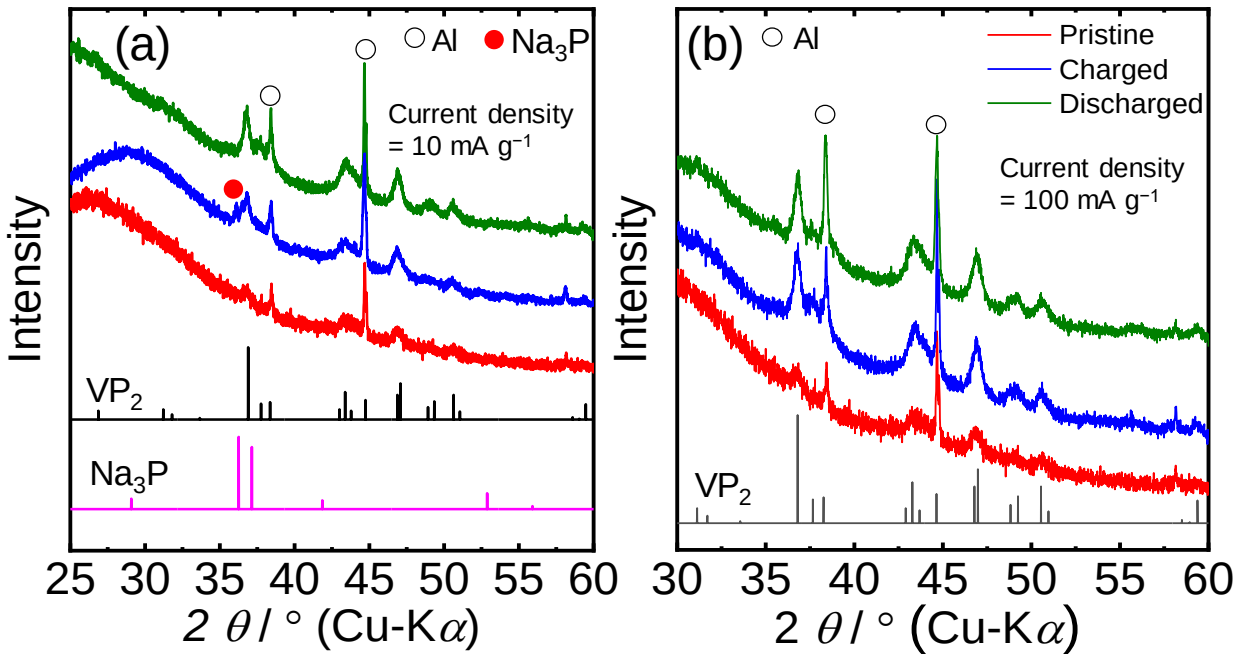

Fig. 6 Ex situ XRD patterns of the VP_2 electrode before and after charge-discharge (pristine, charged to 0.005 V, and discharged to 2.0 V). Current density: (a) 10 mA g^{-1} and (b) 100 mA g^{-1}. The reference patterns of VP_2 and Na_3P are shown for comparison [75, 91].

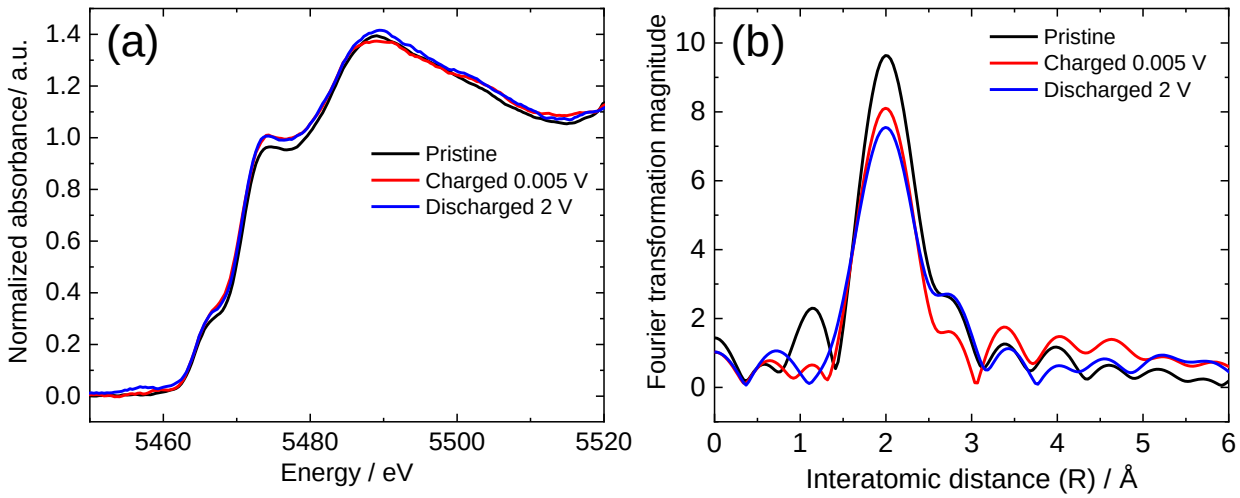

Fig. 7 XAFS analysis data of the VP_2 electrode before and after charge-discharge (pristine, charged to 0.005 V, and discharged to 2.0 V). (a) V *K*-edge XANES spectra, (b) Fourier transforms of the V *K*-edge EXAFS oscillations. Charging-discharging current density = 100 mA g^{-1}.

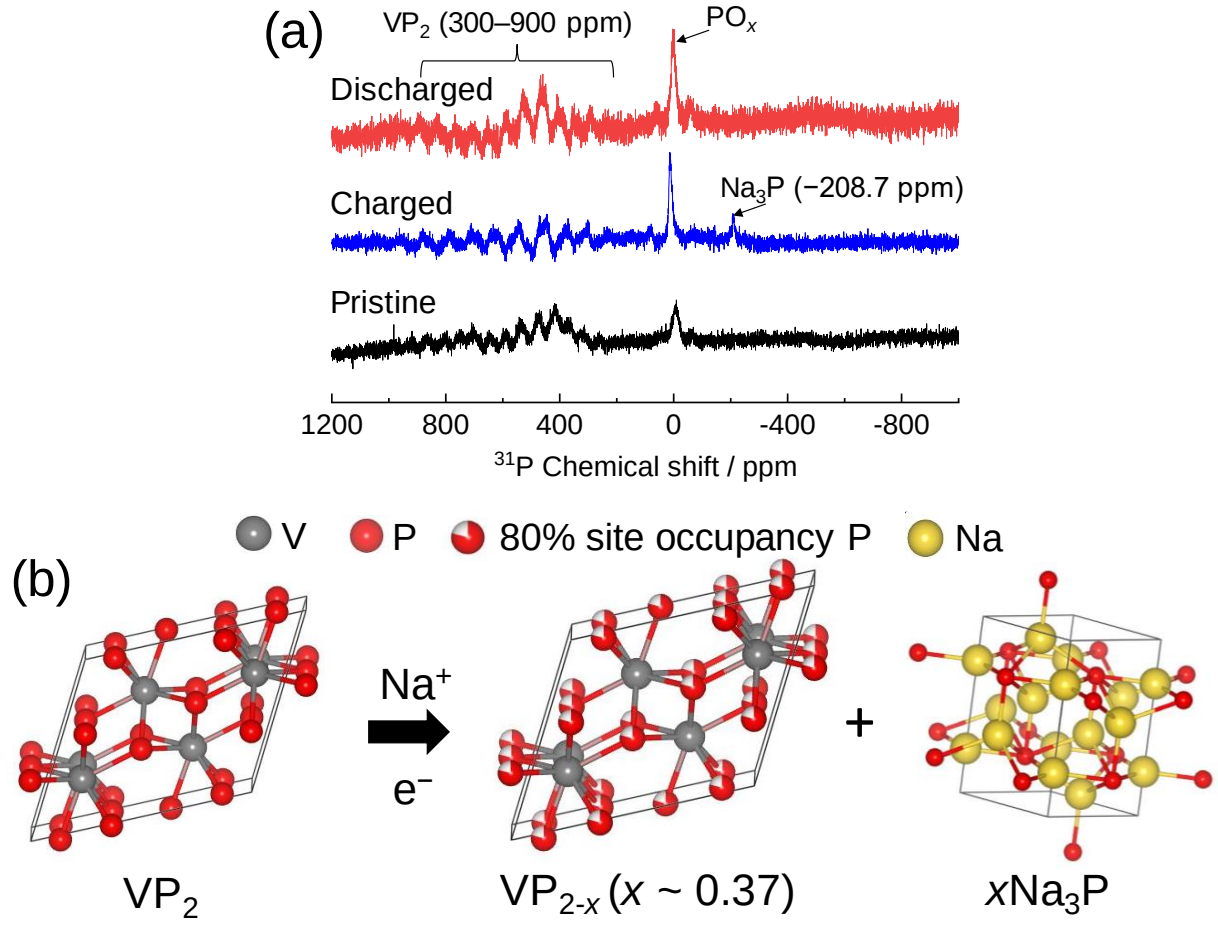

Fig. 8 (a) ^{31}P MAS NMR spectra of VP_2 in pristine powder, charged (0.005 V) and discharged state (2.0 V). The charging and discharging rates were 100 mA g^{-1}. (b) Schematic representation of the conversion reaction mechanism of VP_2.